Wind-Driven South China Sea Deep Basin Warm-Core/ Cool-Core Eddies

Peter C. Chu[1], Yuchun Chen[2] and Shihua Lu[2]

[1]*Naval Postgraduate School, Monterey, California 93943, U.S.A.*
[2]*Institute of Plateau Atmospheric Physics, Academia Sinica, Lanzhou, China*

The formation of the South China Sea (SCS) deep basin warm-core and cool-core eddies was studied numerically using the Princeton Ocean Model (POM) with 20 km horizontal resolution and 23 sigma levels conforming to a realistic bottom topography. Numerical integration was divided into pre-experimental and experimental stages. During the pre-experimental stage, we integrated the POM model for three years from zero velocity and April temperature and salinity climatological fields with climatological monthly mean wind stresses, restoring type surface salt and heat fluxes, and observational oceanic inflow/outflow at the open boundaries. During the experimental stage, we integrated the POM model for another 16 months under three different conditions: one control and two sensitivity runs (no-wind and no lateral transport). We take the fields of the last 12 months for analysis. The simulation under control run agrees well with earlier observational studies on the South China Sea surface thermal variabilities. In addition, the sensitivity study further confirms that the wind effect is the key factor for generation of the SCS deep basin warm/cool eddy and that the lateral boundary forcing is the major factor for the formation of the strong western boundary currents, especially along the southeast Chinese coast during both summer and winter monsoon seasons.

1. Introduction

The South China Sea (SCS) is a semi-enclosed tropical sea located between the Asian land mass to the north and west, the Philippine Islands to the east, Borneo to the southeast, and Indonesia to the south (Fig. 1), a total area of 3.5×10^6 km^2. It includes the shallow Gulf of Thailand and connections to the East China Sea (through the Taiwan Strait), the Pacific Ocean (through the Luzon Strait), the Sulu Sea (through the Mindoro Strait), the Java Sea (through the Gasper and Karimata Straits) and to the Indian Ocean (through the Strait of Malacca). All of these straits are shallow except the Luzon Strait whose maximum depth is 1800 m. The complex topography includes the broad shallows of the Sunda Shelf in the south/southwest; the continental shelf of the Asian landmass in the north, extending from the Gulf of Tonkin to the Taiwan Strait; a deep, elliptical shaped basin in the center, and numerous reef islands and underwater plateaus scattered throughout. The shelf that extends from the Gulf of Tonkin to the Taiwan Strait is consistently near 70 m deep, and averages 150 km in width; the central deep basin is 1900 km along its major axis (northeast-southwest) and approximately 1100 km along its minor axis, and extends to over 4000 m deep. The Sunda Shelf is the submerged connection between southeast Asia, Malaysia, Sumatra, Java, and Borneo and is 100 m deep in the middle; the center of the Gulf of Thailand is about 70 m deep.

Based on limited data sets, both cool and warm pools were detected in SCS (Chu *et al*., 1998). Dale (1956) and Uda and Nakao (1972) reported a cool pool off the central Vietnamese Coast in summer. Nitani (1970) found a cool pool located at the northwest of Luzon. Reports from the South China Sea Institute of Oceanology (SCSIO, 1985) indicate that in the central SCS, a warm pool appears in both summer and winter, but closer to Vietnam in summer at the surface. Recently, a cool pool was detected in the central SCS during 29 December 1993 to 5 January 1994 from the analysis of TOPEX/POSEIDON data (Soong *et al*., 1995).

2. Recent Observational Studies

Based on more complete data sets such as U.S. Navy's Master Oceanographic Observational Data Set (MOODS) and National Centers for Environmental Prediction (NCEP) monthly sea surface temperature (SST) data set, Chu *et al*. (1997a, b) and Chu and Chang (1997) identified SCS seasonal and interannual thermal variabilities. Four patterns, monsoon and transition each with two out-of-phase structures, were found. The monsoon pattern features northeast-

to-southwest oriented isotherms in the northern SCS and a dipole structure in the southern SCS. This southern SCS thermal dipole is opposite from winter to summer: western cool/eastern warm anomaly in winter and the western warm/eastern cool anomaly in summer. The spring-to-summer (fall-to-winter) transition pattern is characterized by the northward expansion of the eastern warm (cool) anomaly and the formation of the central SCS warm (cool) anomaly. Besides, from the NCEP data, Chu *et al.* (1997b) found an evident negative correlation between the wind stress curl and the sea surface temperature anomaly with 1–3 months' leading of the wind stress curl. One of the objectives of this study is to simulate these thermal features using a primitive equation ocean model.

3. A Wind-Driven Mechanism

The bowl-type bottom topography shown in Fig. 1 provides a favorable condition for the formation of eddies in the central SCS basin. If the surface wind stress curl over the central SCS is anticyclonic, Ekman downwelling will occur in the central part of the "bowl" and Ekman upwelling will occur near the boundary of the "bowl" through mass balance. The downwelling prevents the deep cold water from advecting upward, and the upwelling helps the deep cold water advecting upward. The downwelling process is favorable for the formation of warm eddy and the upwelling is favorable for the cool eddy. From late winter to early spring, a surface anticyclonic wind stress curl usually appears over the deep SCS basin, as may be seen from the ensemble mean streamline analysis (Cheang, 1987). This anticyclone generates downwelling in the SCS deep basin and in turn prevents the cold deep water from being advected to the surface. As spring starts the cold northeast monsoon diminishes and the sky over the SCS also enters a more clear period with less cloud cover and rainfall, and rapidly increasing solar radiative warming at the sea surface. The downwelling may
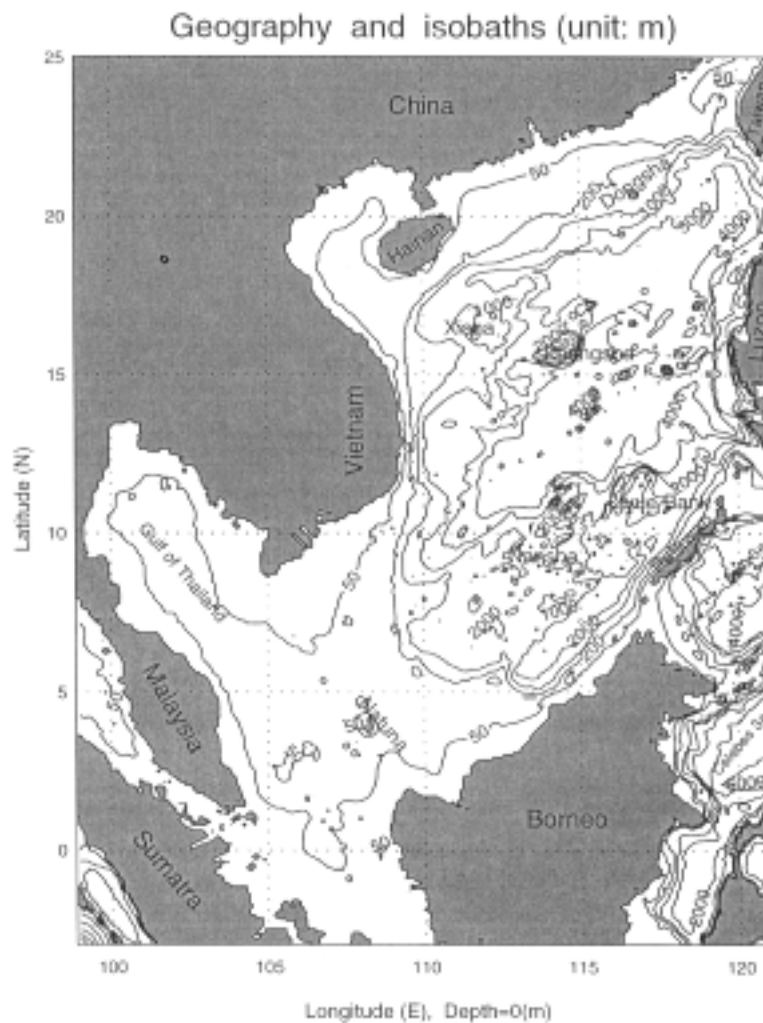

Fig. 1. Bathymetry (km) and coast lines of the South China Sea.

effectively produce a warm pool in the central SCS, as is observed in Chu and Chang (1997), and Chu *et al*. (1997a). This warm pool, with a temperature 1°C higher than the surroundings in a generally warm SCS, may lower the atmospheric surface pressure and promote the onset of the central summer monsoon. The occurrence of a cyclonic circulation with the lower pressure after the onset may then generate Ekman upwelling in the central SCS, bringing the deep cold water into the surface mixed layer. This process may then destroy the warm pool. From late summer to early fall, a surface cyclonic wind stress curl usually appears over the SCS deep basin, as may be seen from the ensemble mean streamline analysis (Cheang, 1987). This cyclone generates

upwelling and in turn drives the cold deep water upward to the surface. The above hypothesis is summarized in a flow chart shown in Fig. 2. This hypothesis may be much too simplistic to represent the real annual cycle of the atmosphere and ocean interaction in the SCS, which is more complicated with many other factors and disturbances involved. There are also unknowns due to lack of data. Nevertheless, certain aspects of the hypothesis suggested in Fig. 2 may be evaluated with a numerical model. In the next section, we will use a numerical model to test the first half of this hypothesis—the development of warm (cool) pool through the anticyclonic (cyclonic) forcing at the surface and the resultant downwelling (upwelling).

4. Numerical Simulations

4.1 Model description

We use the three dimensional primitive equation model developed by Blumberg and Mellor (1987) to simulate the SCS surface thermal variability recently reported (Chu *et al*., 1997a, b) and to investigate the wind effect on the SCS deep basin warm/cool pool formation. The model has the following features: (a) hydrostatic, (b) Boussinesq approximation, (c) a staggered scheme, (d) sigma coordinates in the vertical, (e) a free surface, (f) a second-order turbulence closure model for the vertical viscosity (Mellor and Yamada, 1982), (g) horizontal diffusivity coefficients calculated by the Smagorinsky (1963) parameterization, and (h) split time steps for barotropic (25 seconds) and baroclinic modes (900 seconds).

The model was specifically designed to accommodate mesoscale phenomena commonly found in estuarine and coastal oceanography. Tidal forcing and river outflow were not included in this application of the model. However, the seasonal variation in sea surface height, temperature, salinity, circulation and transport are well represented by the model data. From a series of numerical experiments, the effects of wind forcing and lateral boundary transport on the SCS warm-core and cool-core eddies are analyzed, yielding considerable insight into the external factors affecting the region oceanography.

In this study, we use a rectilinear grid with horizontal spacing of 20 km by 20 km resolution and 23 vertical sigma coordinate levels. The model domain is from 3.06°S to 25.07°N, and 98.84°E to 121.16°E, which encompasses the SCS and the Gulf of Thailand, and uses realistic bathymetry data from the Naval Oceanographic Office DBDB5 database (5 minute by 5 minute resolution). Consequently, the model contains $125 \times 162 \times 23$ horizontally fixed grid points (Fig. 3). The horizontal diffusivities are modeled using the Smagorinsky (1963) form with the coefficient chosen to be 0.2 for this application. The bottom stress is assumed to follow a quadratic law and the drag coefficient is specified as 0.0025 (Blumberg and Mellor, 1987).
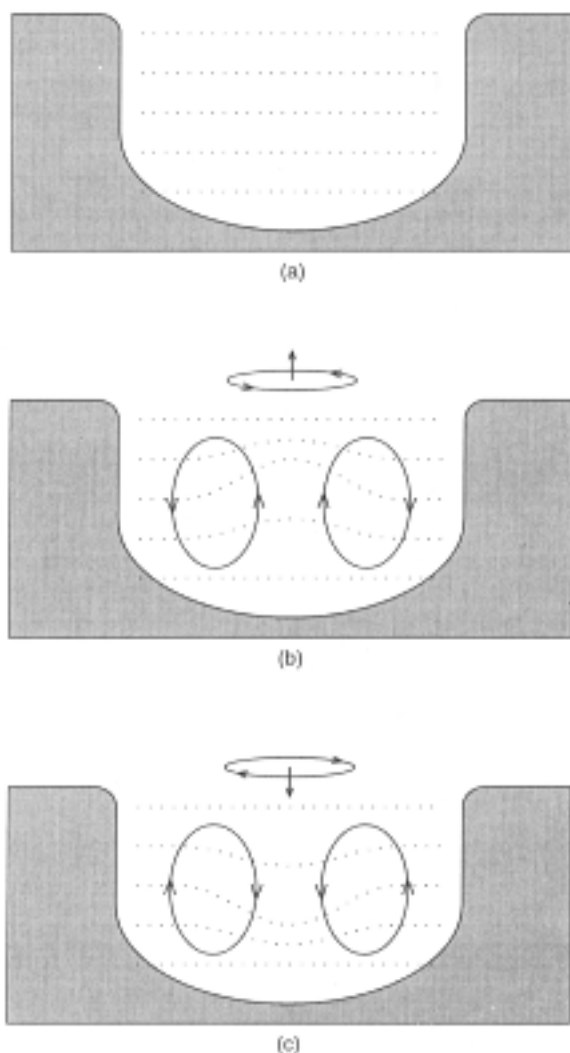

Fig. 2. A wind effect for the formation of the SCS deep basin warm and cool pools: (a) no wind forcing, (b) cool pool generated by the surface cyclonic wind stress curl, and (c) warm pool generated by the surface anticyclonic wind stress curl. The dotted lines are isotherms decreasing with depth.

4.2 Atmospheric forcing
Wind forcing

The atmospheric forcing for the SCS application of the POM includes mechanical and thermodynamical forcing. The wind forcing is depicted by

Fig. 3. The model horizontal grid.

$$\rho_0 K_{\mathrm{M}}(\partial u/\partial z, \partial v/\partial z)_{z=0} = (\tau_{0x}, \tau_{0y}) \qquad (1)$$

where (u, v) and (τ_{0x}, τ_{0y}) are the two components of the water velocity and wind stress vectors, respectively. The wind stress at each time step is interpolated from monthly mean climate wind stress (Hellerman and Rosenstein, 1983), which was taken as the value at the middle of the month. SCS experiences two monsoons, winter and summer, every year. During the winter monsoon season, a cold northeast wind blows over SCS (Fig. 4(b)) as a result of the Siberian high pressure system located over the east Asian continent. Radiative cooling and persistent cold air advection maintain cold air over SCS. The northeast-southwest oriented jet stream is positioned at the central SCS. Such a typical winter monsoon pattern lasts nearly 6 months (November to April). During the summer monsoon season, a warm and weaker southwest wind blows over SCS (Fig. 4(a)). Such a typical summer monsoon pattern lasts nearly 4 months (mid-May to mid-September). The mean surface wind stress over central portion of SCS is nearly 0.2 N/m² in January (Fig. 4(b)) and is approximately 0.1 N/m² in July (Fig. 4(a)).

The seasonal variation of wind stress curl over the SCS warm-core/cool-core eddy formation area (around 6°–20°N, 110°–120°E) is represented by the interchange of the two basic patterns: winter and summer (Fig. 5). The winter pattern is featured by an anticyclonic curl (Fig. 5(a)) and the summer pattern is characterized by a cyclonic curl (Fig. 5(c)). The spring-to summer (Fig. 5(b)) and fall-to-winter (Fig. 5(d)) patterns are transitions of the two basic patterns.

Thermal forcing
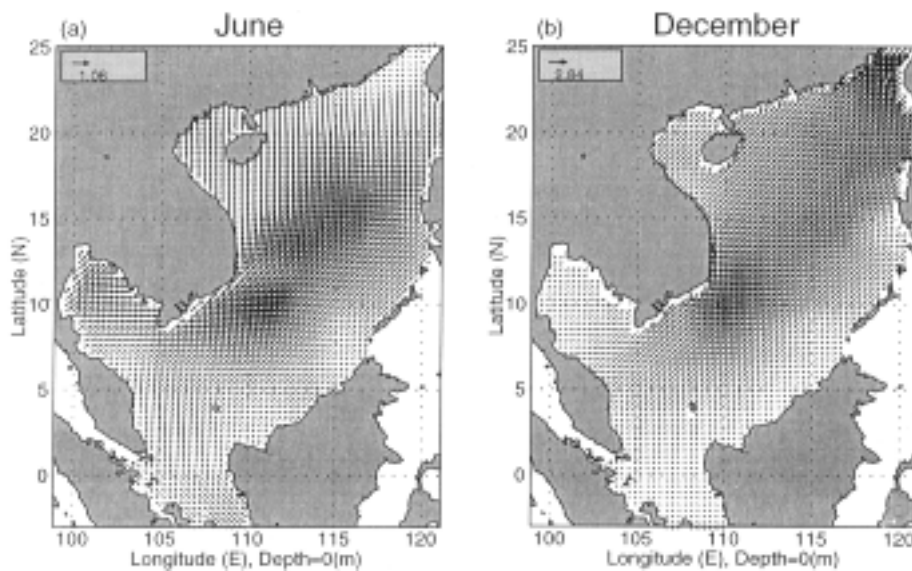
Surface thermal forcing is depicted by

Fig. 4. Climatological wind stress (0.1 N m⁻²) for (a) June, and (b) December (after Hellerman and Rosenstein, 1983).

$$K_{\text{H}} \frac{\partial \theta}{\partial z} = \alpha_1 \left(\frac{Q_{\text{H}}}{\rho c_p} \right) + \alpha_2 C (\theta_{\text{OBS}} - \theta) \qquad (2)$$

$$K_{\text{S}} \frac{\partial S}{\partial z} = \alpha_1 Q_{\text{S}} + \alpha_2 C (S_{\text{OBS}} - S) \qquad (3)$$

where θ_{OBS} and S_{OBS} are the observed surface potential temperature and salinity, c_p is the specific heat, and Q_{H} and Q_{S} are surface net heat and salinity fluxes, respectively. The relaxation coefficient C is the reciprocal of the restoring time period for a unit volume of water. The parameters (α_1, α_2) are (0,1)-type switches: $\alpha_1 = 1$, $\alpha_2 = 0$, would specify only flux forcing is applied; $\alpha_1 = 0$, $\alpha_2 = 1$, would specify that only restoring type forcing (Haney, 1971) is applied. In this study, the surface thermal forcing is determined solely by restoring forcing, that is $\alpha_1 = 0$ and $\alpha_2 = 1$ in Eqs. (2) and (3). The relaxation coefficient C is taken to be 0.7 m/day, which is equivalent to a relaxation time of 43 days for an upper layer 30 m thick (Chu *et al.*, 1996).

4.3 Lateral boundary conditions

Solid lateral boundaries, i.e., the modeled ocean bordered by land, were defined using a free slip condition for velocity and a zero gradient condition for temperature and
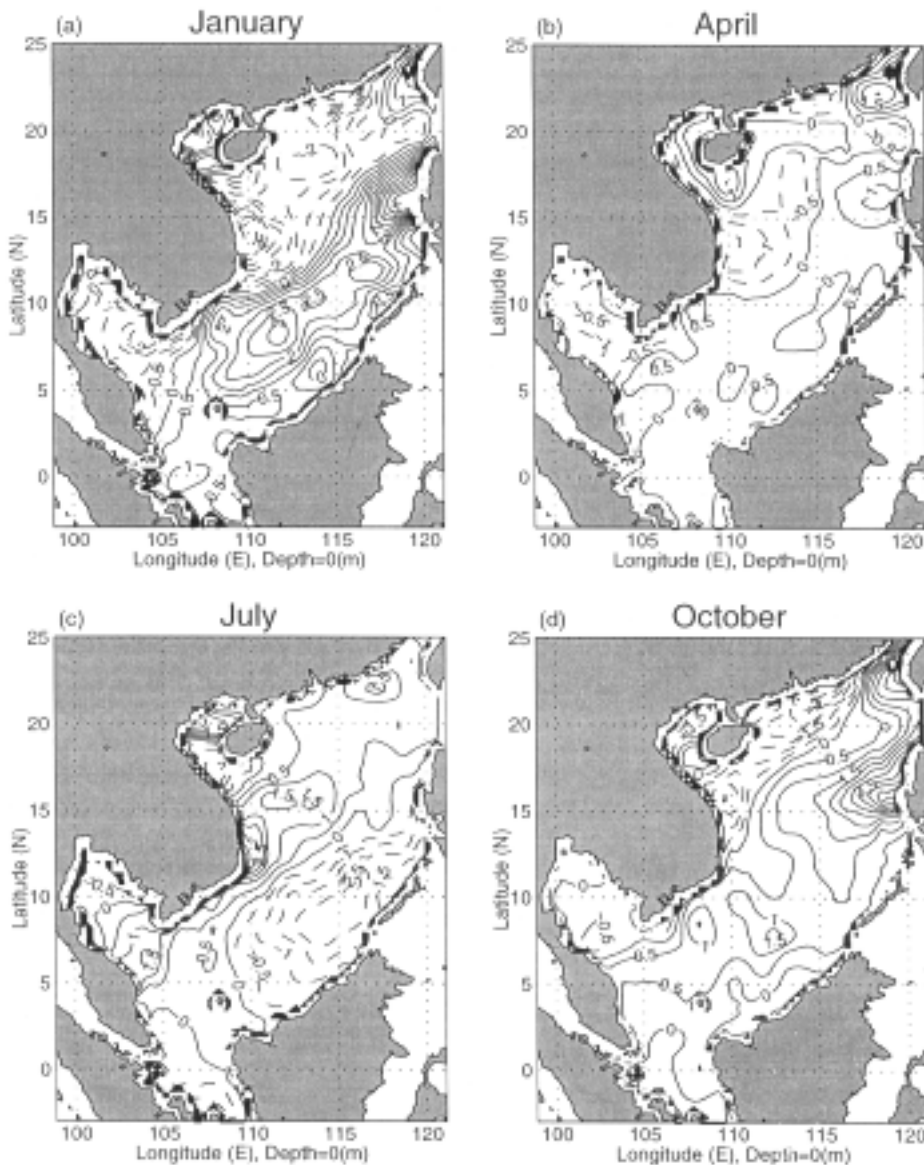

Fig. 5. Climatological wind stress curl (10^{-10} N m^{-3}) for (a) January, (b) April, (c) July, and (d) October (after Hellerman and Rosenstein, 1983). Here, the solid (dashed) curves denote positive (negative) values.

salinity. No advective or diffusive heat, salt or velocity fluxes occur through these boundaries.

Open boundaries, where the numerical grid ends but the fluid motion is unrestricted, were treated as radiative boundaries. Volume transport through the Luzon Strait, Taiwan Strait, and Gasper/Karimata Strait was defined according to observations (Table 1). However, the Balabac Channel, Mindoro Strait, and Strait of Malacca are assumed to have zero transport. When the water flows into the model domain, temperature and salinity at the open boundary are likewise prescribed from the climatological data (Boyer and Levitus, 1994). When water flows out of the domain, the radiation condition was applied,

$$\frac{\partial}{\partial t}(\theta, S) + U_n \frac{\partial}{\partial n}(\theta, S) = 0 \qquad (4)$$

where the subscript n is the direction normal to the boundary.

Through a recent integration of a global 1.5-layer reduced gravity model with 1/2 resolution, Metzger and Hurlburt (1996) successfully simulated the mass exchange between the SCS, the Sulu Sea, and the Pacific Ocean. We might use the global model results to establish the open boundary conditions in the future.

4.4 Initial conditions and initialization

The model year consists of 360 days (30 days per month), day 361 corresponds to 1 January. Numerical integration was divided into pre-experimental and experimental stages. During the pre-experimental stage, we integrated the POM model for three years from zero velocity and April temperature and salinity climatological fields (Levitus and Boyer, 1994; Levitus *et al.*, 1994) with climatological monthly mean wind stresses (Hellerman and Rosenstein, 1983), restoring type surface salt and heat fluxes ($\alpha_1 = 0$, $\alpha_2 = 1$), and observational oceanic inflow/outflow at the open boundaries.

4.5 Experiment design

During the experimental stage, we integrated the POM model for another 16 months from the end of the pre-experimental stage for three different cases. Case 1 was the control run (same conditions taken as in the pre-experimental stage), Case 2 was the no-wind run, and Case 3 was the no-lateral transport run. The difference between the control and the no-wind runs should represent the wind forcing effect. The difference between the control and the no-lateral transport runs should represent the lateral transport effect. Only the simulated fields for the last 12 month data were used for discussion (Fig. 6).

Since Chu *et al.* (1997b) found an evident correlation from the NCEP data between the cyclonic (anticyclonic) wind stress curl and the high (low) sea surface temperature
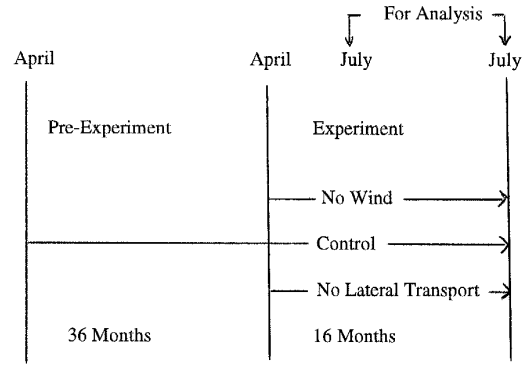

Fig. 6. Two stages of numerical integration.

anomaly with a season's leading of the wind stress curl, we may expect that the model simulates a central SCS warm (cool) pool in spring (fall).

5. Annual Mean Upper Level Temperature Field

Since the surface thermal forcing is determined solely by restoring forcing in this study, we chose 30-m as a representative depth for presenting the upper ocean temperature field. The simulated 12-month mean temperature field from the control run reveals the following features (Fig. 7(a)): (a) northeast-southwest oriented isotherms with temperature decreasing from 27.5°C near the southern boundary to 24°C near the southeast China coast (a weak temperature gradient), (b) warm-cool-warm (W-C-W) structure in southern SCS (south of 10°N) with a cool pool (<27°C) near Natuna Island sandwiched by two warm pools (≥27°C) located at southeast of the deep basin (112°–120°E, 5°–10°N) and southern shelf area from Gulf of Thailand to Karimata Strait, and (c) meso-scale cool-core eddies in northern SCS (north of 10°N). This pattern agrees well with an earlier observational study on the South China Sea surface temperature (Chu *et al.*, 1997b).

The upper level (30-m) annual mean thermal field is quite sensitive to the wind forcing especially in northern SCS, where several meso-scale eddies occur in the control run (Fig. 7(a)) and in the no-lateral transport run (Fig. 7(c)), but none in the no-wind run (Fig. 7(b)). This indicates that the wind forcing is the key factor for generating meso-scale eddies.

6. Seasonal Variation of the Upper Level Temperature Field

6.1 Central SCS warm/cool pool

Monthly mean temperature anomaly ($\tilde{T}$) was computed by subtracting the annual mean temperature from monthly mean temperature. The simulated $\tilde{T}$ field at 30-m depth has a strong seasonal variation, which can be easily seen from the control run (Fig. 8).
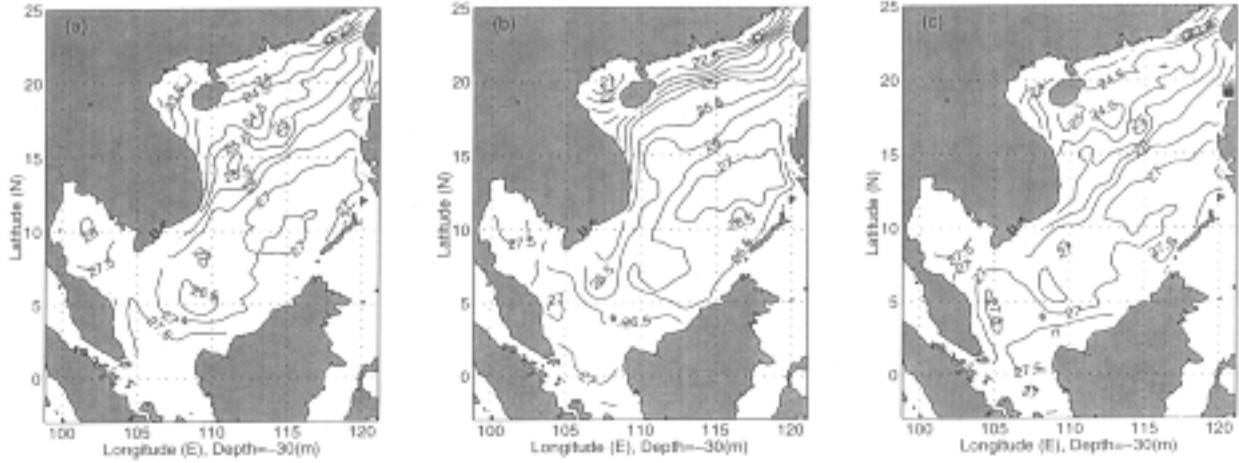
Fig. 7. Annual mean temperature field at 30-m depth: (a) control run, (b) no-wind run, and (c) no-lateral transport run.

(1) The winter (Fig. 8(a)) pattern shows negative values of $\tilde{T}$ occupying the whole SCS except narrow coastal zones (e.g., southeast China coast, southeast Vietnam coast, Thailand Gulf coast, and western Borneo coast) and small areas in central and northern SCS. A small warm anomaly ($\tilde{T} \geq 0°C$) occurs in central SCS near southern Vietnam coast. In southern SCS (south of 10°N), $\tilde{T}$ has W-C-W pattern with a cool pool ($\tilde{T} \leq -1.5°C$) near Natuna Island sandwiched by two warm pools ($\geq -1°C$) located at southeast of the deep basin and southern shelf area from Gulf of Thailand to Karimata Strait. This pattern coincides with the annual southern SCS W-C-W pattern, which indicates the enhancement of the southern SCS W-C-W pattern in winter.

(2) The spring-to-summer transition (Fig. 8(b)) pattern shows *a warm pool formation* at western part of the SCS deep basin (10°–16°N, 110°–115°E) with the maximum anomaly of 1°C. Southern SCS $\tilde{T}$ has an evident W-C-W pattern with a cool pool ($\tilde{T} \leq -2°C$) near Natuna Island sandwiched by two warm pools ($\tilde{T} \geq -1°C$) located at southeast of the deep basin and southern shelf area from Gulf of Thailand to Karimata Strait ($\tilde{T} > -0.5°C$).

(3) The summer pattern (Fig. 8(c)) shows the expansion of the central SCS warm pool. Positive values of $\tilde{T}$ occupies vast SCS area except western central SCS and coastal region of Gulf of Thailand. A central SCS cool pool occurs near the South Vietnam coast with the minimum value of –1°C. In southern SCS, $\tilde{T}$ has an evident C-W-C pattern with a warm pool ($\tilde{T} \geq 2°C$) near Natuna Island sandwiched by two cool pools located at southeast of the deep basin ($\tilde{T} \leq 1°C$) and southern shelf area from Gulf of Thailand ($\tilde{T} \leq -0.5°C$) to Karimata Strait ($\tilde{T} \leq 0.5°C$).

(4) The fall-to-winter transition (Fig. 8(d)) pattern shows *a cool pool formation* at the SCS deep basin with the maximum anomaly of –1°C. The southern SCS has an evident C-W-C pattern with a warm pool ($\tilde{T} \geq 1.5°C$) near the Natuna Island sandwiched by two cool pools located

southeast of the deep basin ($\tilde{T} \leq 1°C$) and the shelf of Gulf of Thailand to Karimata Strait ($\tilde{T} \leq 0.5°C$).

Thus, four patterns, monsoon and transition each with two opposite structures, were simulated. The winter (summer) monsoon season is characterized by (a) dominance of cool (warm) anomaly in the vast SCS basin, (b) formation of weak warm (cool) anomaly in central SCS near South Vietnam Coast, and (c) southern SCS W-C-W (C-W-C) pattern. The spring-to-summer (fall-to-winter) transition is featured by the occurrence of warm (cool) pool in the central SCS. The simulated seasonal variation agrees well with earlier observational study (Chu *et al.*, 1997b).

6.2 Wind-driven central SCS warm/cool pool

We compare the upper level (30-m) temperature fields among the three experiments to identify the forcing for the generation of the central SCS warm/cool pool. The simulated $\tilde{T}$ field at 30-m depth for the no-wind run shows a very weak central SCS warm pool ($\tilde{T} < 0.5°C$) during the spring-to-summer transition (Fig. 9(b)) and no central SCS cool pool during the fall-to-winter transition (Fig. 9(d)). However, the simulated $\tilde{T}$ field at 30-m depth for the no-lateral transport run (Fig. 10) shows a very similar pattern during the two transition seasons: occurrence of the central SCS warm pool during the spring-to-summer transition (Fig. 10(b)) and appearance of the central SCS cool pool during the fall-to-winter transition (Fig. 10(d)). This suggests that the wind forcing is the key factor for the formation of the central SCS warm/cool pool.

7. Upper Level Current Structure

7.1 Vietnam coastal jet and multi-eddy structure

During the winter monsoon period (November to March) the Asian high pressure system brings strong winds from the northeast and the SCS upper layer (30-m depths) basin-scale
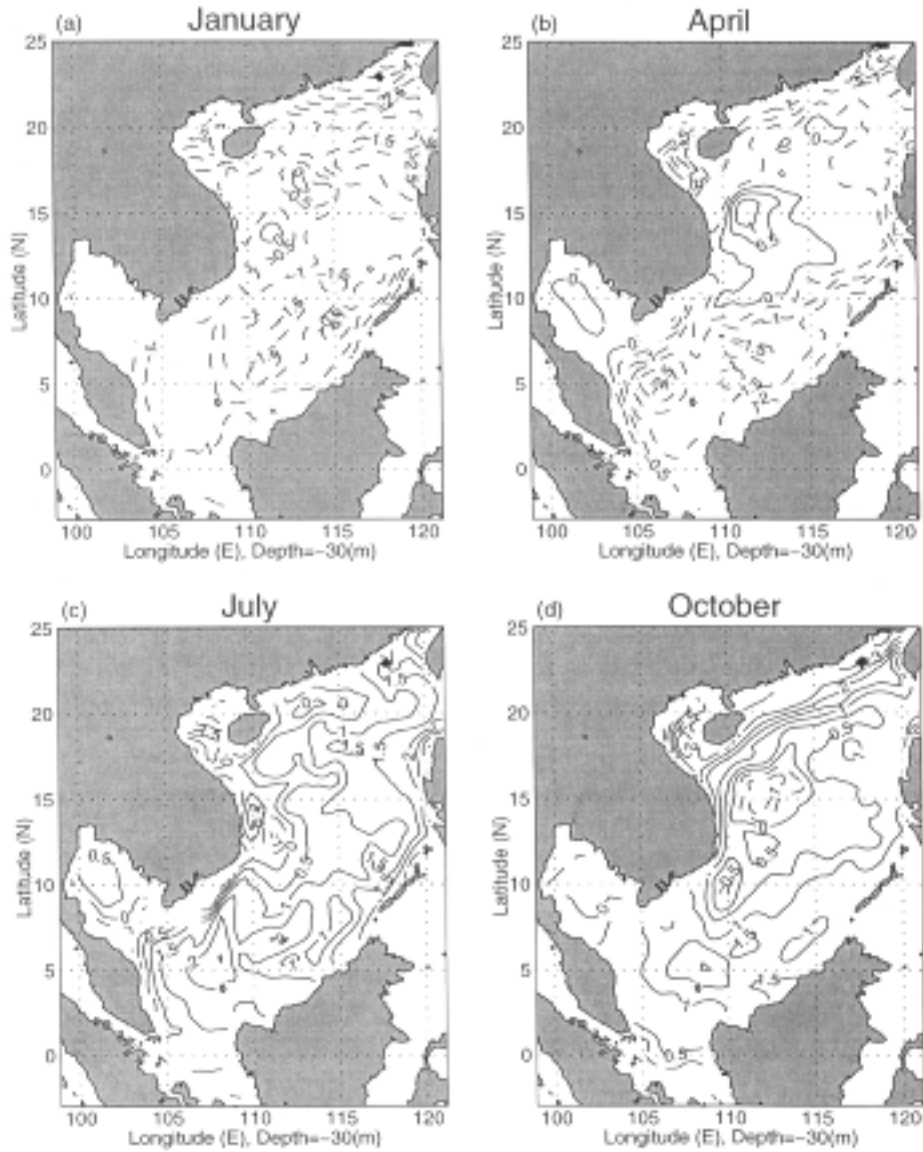
Fig. 8. Monthly temperature anomaly at 30-m depth for the control run: (a) January, (b) April, (c) July, and (d) October. Here, the solid (dashed) curves denote positive (negative) values.

circulation pattern is cyclonic (Fig. 11(a)). Inflow from the Bashi Channel (the Kuroshio intrusion) and Strait of Taiwan augments currents southwest along the Asian continental shelf, then south along the coast of Vietnam and eventually out through the Gasper and Karimata Straits in the south. Western intensification of the general cyclonic circulation pattern was also simulated. From the south coast of Hainan Island, the current intensifies as it flows from north to south along the Vietnam coast. Average speed is around 0.92 m/s in the core. A strong cyclonic eddy appears with the maximum tangential velocity of around 0.6 m/s, located in the northeast (3°–10°N, 108°–113°E) of the Natuna Island.

We may call it the Natuna Island Eddy (NIE). As winter progresses, near surface currents along the coast of Borneo begin to turn northwest, eventually flowing directly away from the coastline and into the Natuna eddy where the southern edge of the deep basin meets the Sunda Shelf; the south extension of the Vietnam Coastal Jet (VCJ) veers west.

During the spring-to-summer transition (Fig. 11(b)), the southward VCJ weakens and a strong anticyclonic eddy occurs in the central SCS (13°–17°N, 109°–117°E) with the maximum tangential velocity of 0.5 m/s and is surrounded by several cyclonic eddies. Comparing Fig. 11(b) to Fig.
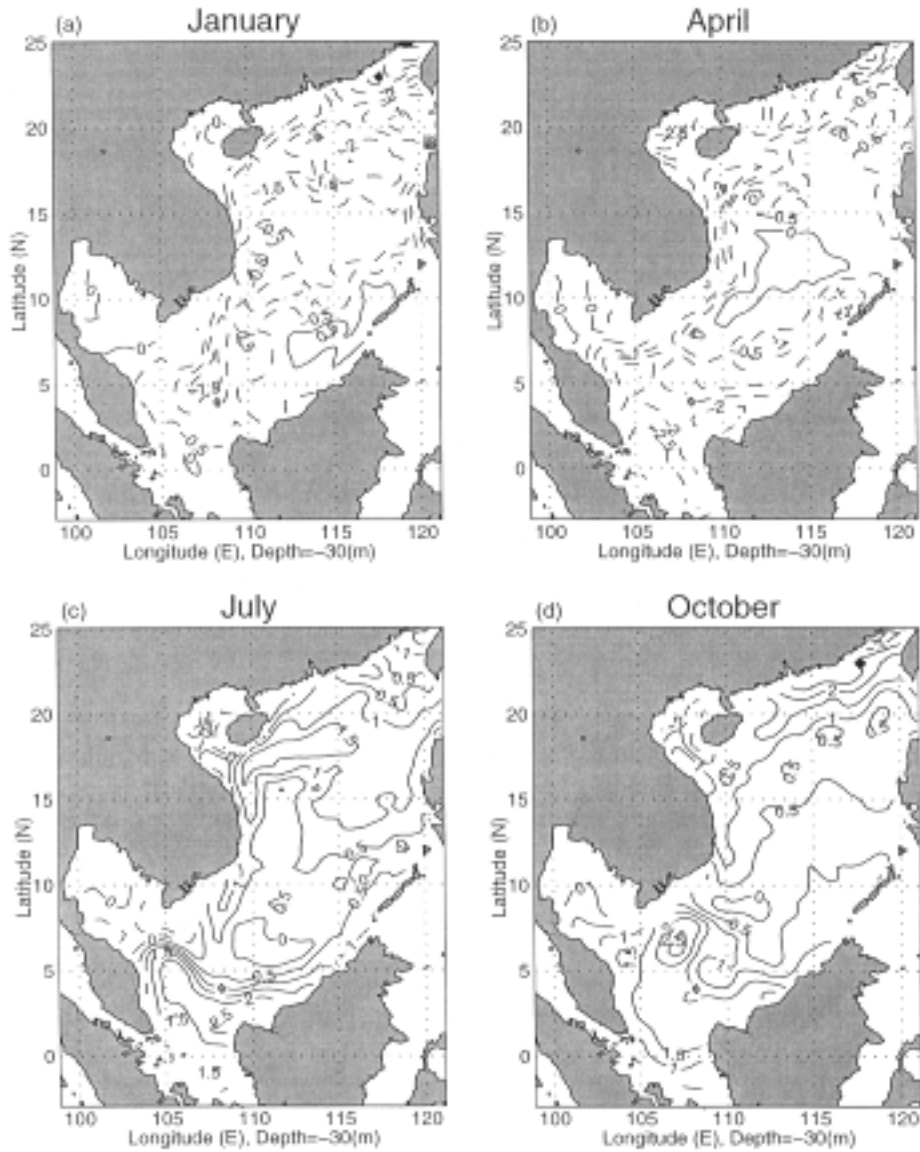
Fig. 9. Monthly temperature anomaly at 30-m depth for the no-wind run: (a) January, (b) April, (c) July, and (d) October. Here, the solid (dashed) curves denote positive (negative) values.

8(b), we see that this anticyclonic eddy is co-located with the central SCS warm pool. In the southern SCS, the weakening NIE is spited into dual cyclonic eddies, located at northeast (5°–7°N, 108°–112°E) and northwest (3°–6°N, 105°–108°E) of the Natuna Island, respectively.

During the summer monsoon period (May to September) winds blow from the southwest and the SCS surface circulation generally follows suit with anticyclonicity in the southern basin (Fig. 11(c)). Inflow is through the southern Gaspar and Karimata Straits and outflow is through the northern Taiwan Strait and eastern Bashi Channel (Table 1). Velocities reach 1.0 m/s at the peak of the summer monsoon

within VCJ with a summer average value of 0.5 m/s. The western boundary current splits and partially leaves the coast; the bifurcation point is at 10°N in July (Fig. 11(c)). The central SCS anticyclonic eddy weakens drastically.

During the fall-to-winter transition (Fig. 11(d)), the southward VCJ establishes and an evident cyclonic eddy occurs in the central SCS (12°–20°N, 109°–115°E). The western flank of this cyclonic eddy joins the VCJ with the maximum tangential velocity of 0.88 m/s. and is surrounded by several cyclonic eddies. Comparing Fig. 11(d) to Fig. 8(d), we see that this cyclonic eddy is co-located with the central SCS cool pool.
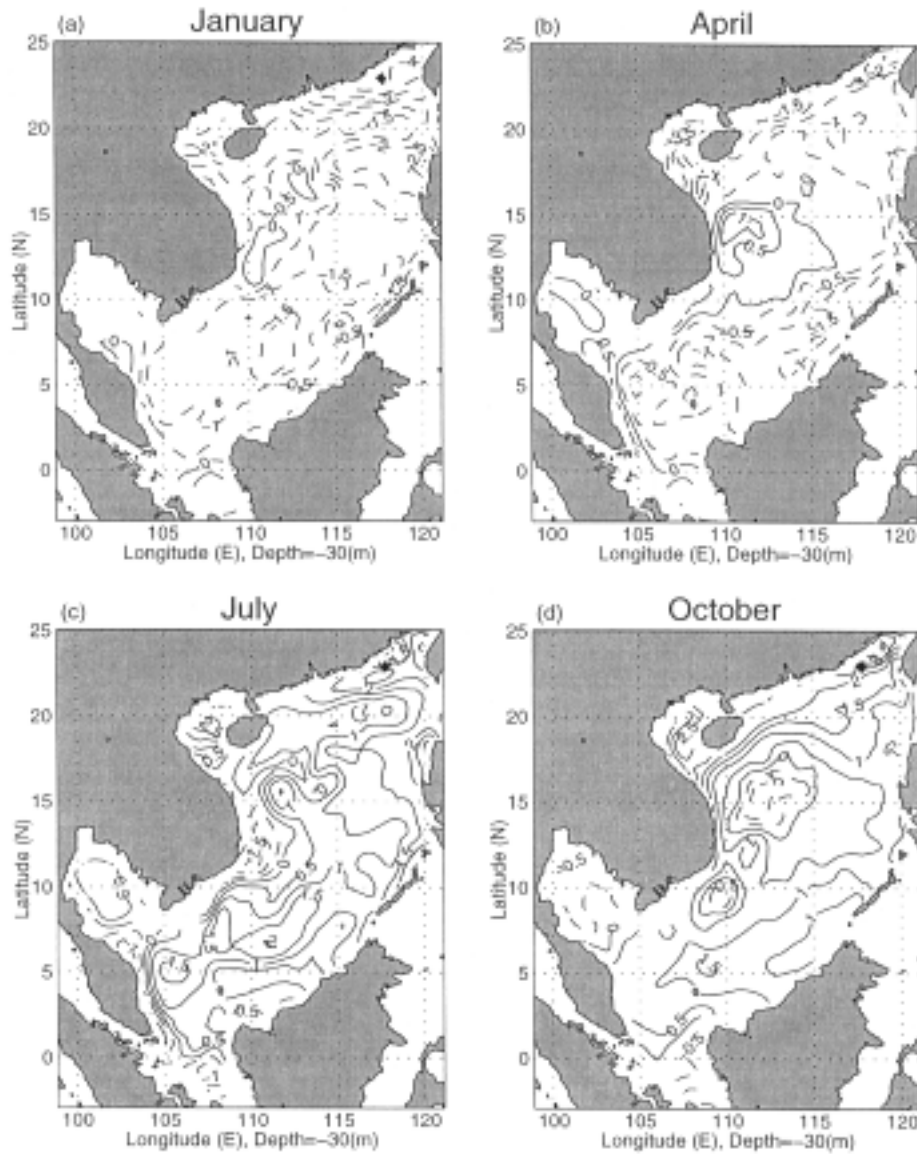
Fig. 10. Monthly temperature anomaly at 30-m depth for the no lateral transport run: (a) January, (b) April, (c) July, and (d) October. Here, the solid (dashed) curves denote positive (negative) values.

7.2 Mechanisms for the central SCS anticyclonic/cyclonic eddy formation

We compare the upper level (30-m) velocity fields among the three experiments to identify the forcing for the generation of the central SCS anticyclonic/cyclonic eddy during the transition seasons. To do so, we computed two velocity difference fields: (a) control minus no-wind runs (Fig. 12) indicating the wind effect, and (b) control minus no-lateral transport runs (Fig. 13) indicating the lateral transport effect.

Wind effect

Comparing Fig. 12 to Fig. 8, we find the wind effects on the circulation. During the winter monsoon season (Figs.

12(a) and 8(a)), the wind effect causes the NIE formation, and contributed a small portion (around 20%) of southward VCJ formation. During the spring-to-summer transition (Figs. 12(b) and 8(b)), the wind forcing causes the *formation of the central SCS anticyclonic eddy* ($13°$–$17°$N, $109°$–$117°$E) with the maximum tangential velocity of 0.4 m/s. During the summer monsoon season (Figs. 12(c) and 8(c)), the wind forcing contributes nearly 40% of the northward western boundary currents (i.e., VCJ) in the south of $10°$N and generates a southwestward to southward recirculating current (not appeared in the control run) along the southeast Chinese coast to central Vietnamese coast in the north of $10°$N (Fig. 12(c)). During the fall-to-winter transition, the
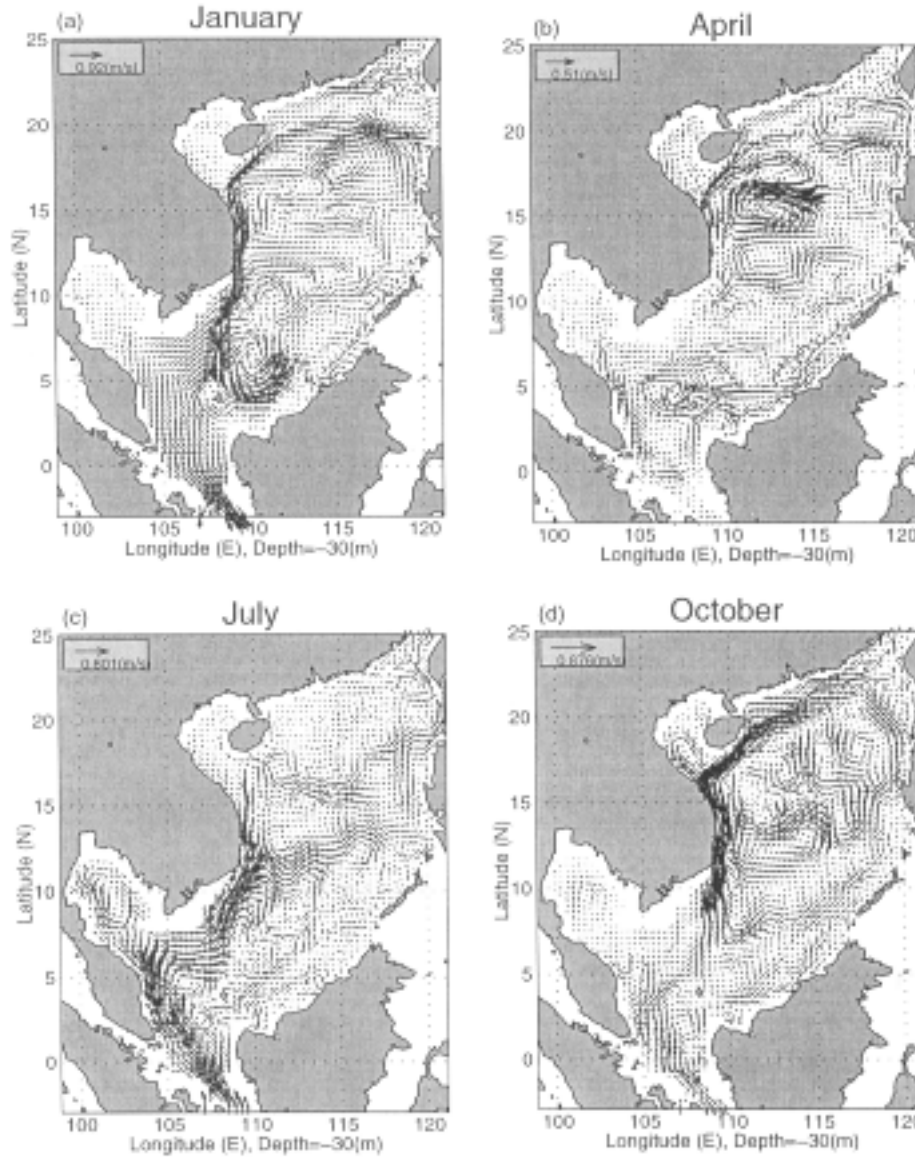
Fig. 11. Monthly horizontal current vectors at 30-m depth for the control run: (a) January, (b) April, (c) July, and (d) October.

wind forcing causes the *formation of the central SCS cyclonic eddy* (12°–20°N, 109°–115°E) with the maximum tangential velocity of 0.8 m/s, and contributes more than 90% of the formation of the southwestward to southward western boundary currents along the southeast Chinese and Vietnamese coasts.

Besides, the wind effect turns the most portion of the western boundary current to the east around 5°N in winter (Fig. 12(a)) and separates the northward boundary current from the coast at 12°N and 16°N in summer (Fig. 12(c)).
Lateral boundary effect

Comparing Fig. 13 to Fig. 8, we find the effects of the lateral boundary transport on the circulation pattern. During the winter monsoon season (Figs. 13(a) and 8(a)), the lateral

boundary forcing is the major factor (80%) to the *formation of the strong western boundary currents* especially along the southeast Chinese coast. Besides, it also contributes to the NIE formation. During the spring-to-summer transition (Figs. 13(b) and 8(b)), the lateral boundary forcing generates a cyclonic-anticyclonic dipole in the central SCS (13°–17°N, 109°–117°E) with the maximum tangential velocity of 0.25 m/s, which indicates the *weakening (enhancing) the western (eastern) half of the central SCS anticyclonic eddy* (Fig. 8(b)). During the summer monsoon season (Figs. 13(c) and 8(c)), the lateral boundary forcing is the major contributor to the *formation of the northward western boundary currents* along the Vietnamese coast with several mesoscale anticyclonic recirculating eddies. The strong north to

Table 1. Bi-monthly variation of volume transport (Sv) at the lateral open boundaries. The positive/negative values mean outflow/ inflow and were taken from Wyrtki (1961).

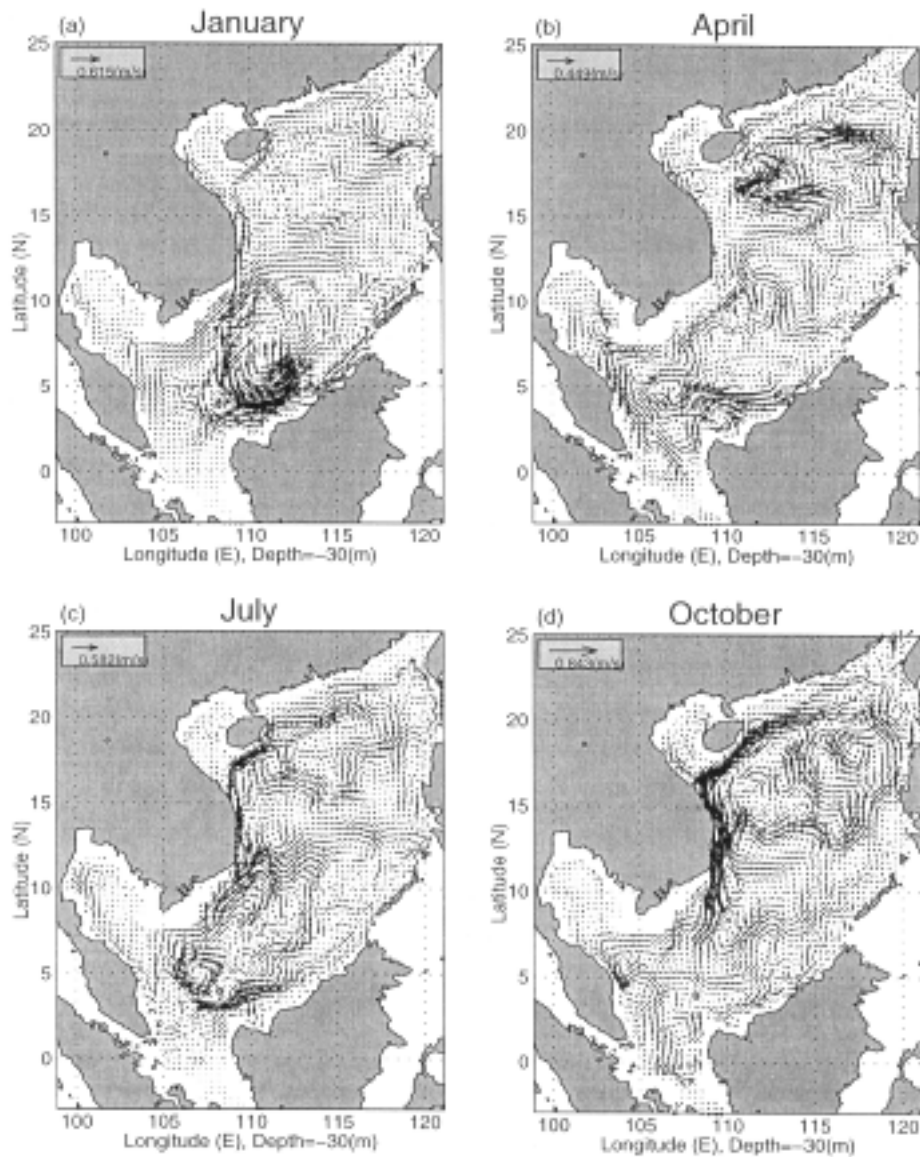| Month	Feb.	Apr.	Jun.	Aug.	Oct.	Dec.
Gaspar-Karimata Straits	4.4	0.0	−4.0	−3.0	1.0	4.3
Luzon Strait	−3.5	0.0	3.0	2.5	−0.6	−3.4
Taiwan Strait	−0.9	0.0	1.0	0.5	−0.4	−0.9

Fig. 12. Monthly horizontal current vector differences (control minus no-wind runs) at 30-m depth for the control run: (a) January, (b) April, (c) July, and (d) October.

northeastward boundary current along the Vietnamese coast north to 10°N and the southeast Chinese coast (Fig. 13(c)) will balance the southwestward to southward recirculating current generated by the wind forcing (Fig. 12(c)). During

the fall-to-winter transition, the lateral boundary forcing does not contribute to the formation of southward VCJ (Fig. 13(d)). But, it generates a cyclonic-anticyclonic dipole in the central SCS (10°–15°N, 109°–117°E) with the maxi-
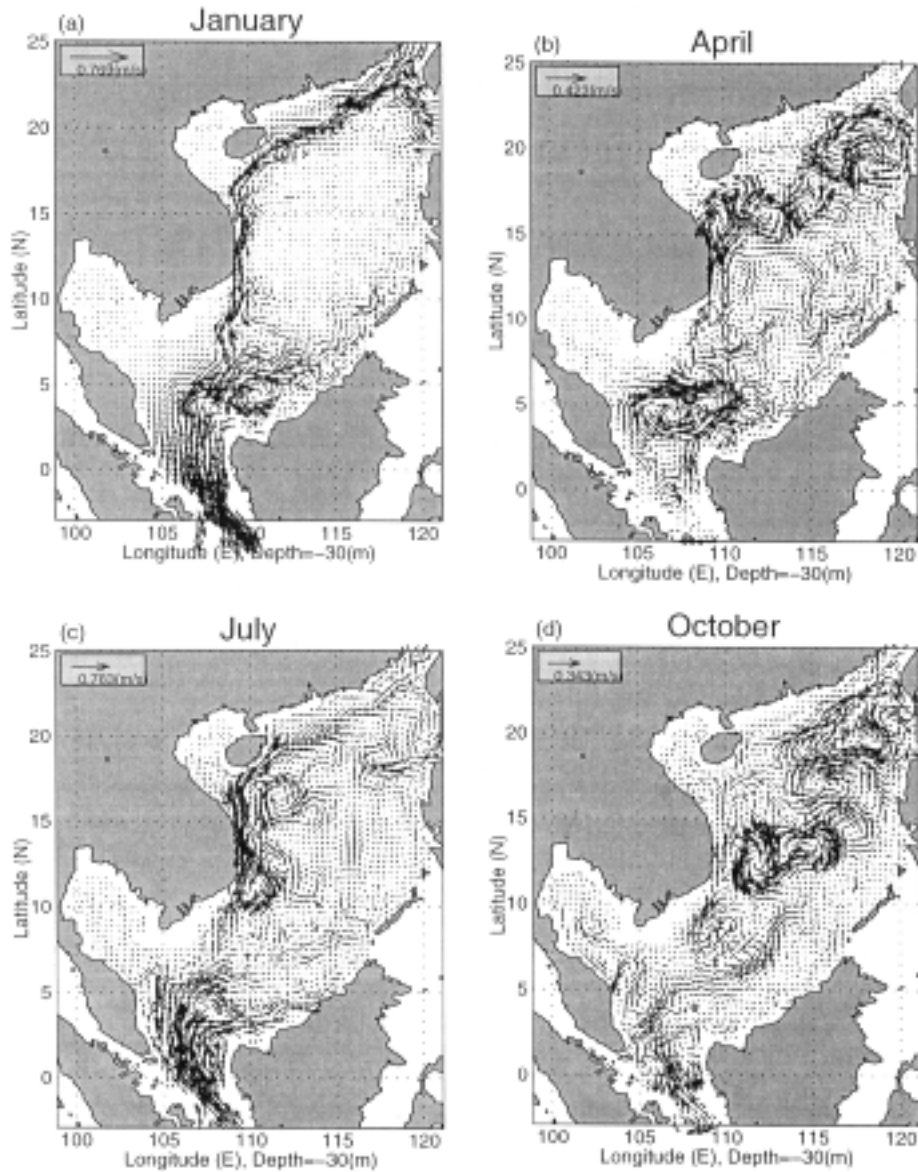
Fig. 13. Monthly horizontal current vector differences (control minus no lateral transport runs) at 30-m depth for the control run: (a) January, (b) April, (c) July, and (d) October.

mum tangential velocity of 0.3 m/s, which indicates the *weakening (enhancing) the eastern (western) half of the central SCS cyclonic eddy* (Fig. 8(d)).

8. Conclusions

(1)   We simulated the South China Sea circulation and thermohaline variability using the Princeton Ocean Model. The simulation agrees well with earlier observational studies on the MOODS and NCEP data (Chu *et al*., 1997a, b). The simulated 12-month mean upper level (30-m depth) temperature field shows northeast-southwest oriented isotherms with a weak temperature gradient, a cool pool near Natuna Island, and a warm pool located southeast of the deep basin

(112°–120°E, 5°–10°N). The simulated seasonal variation shows the formation of the SCS deep basin warm (cool) anomaly in the spring-to-summer (fall-to-winter) transition season.

(2)   We verified the wind effect for the SCS deep basin warm/cool eddy generation using the POM model under the climatological forcing. The results show that the deep SCS basin anticyclonic (cyclonic) surface wind stress curl in winter (summer) generates a major warm anticyclonic (cool cyclonic) eddy during spring (fall) with the maximum tangential velocity of 0.4 (0.8) m/s and temperature anomaly of 1°C (–1°C).

(3)   During the winter monsoon season, the wind ef-

fect contributes a small portion (around 20%) for the formation of southward Vietnamese Coastal Jet in the most part, but it turns the most portion of the western boundary current to the east around 5°N. During the summer monsoon season, the wind effect contributes nearly 40% of the northward Vietnamese Coastal Jet in the south of 10°N, separates the northward boundary current from the coast at 12°N and 16°N, and generates a southwestward to southward recirculating current along the southeast Chinese coast to central Vietnamese coast in the north of 10°N. This recirculating boundary current is counter-balanced by the lateral boundary forcing.

(4) We also verified the lateral boundary forcing effect on the SCS circulation and thermal variability. The results show that the lateral boundary forcing is the major factor to the formation of the strong western boundary currents especially along the southeast Chinese coast during both summer and winter monsoon seasons. It weakens (enhances) the western (eastern) half of the central SCS anticyclonic eddy during the spring-to-summer transition period and weakens (enhances) the eastern (western) half of the central SCS cyclonic eddy during the fall-to-winter transition period.

(5) Future studies should concentrate on less simplistic scenarios. Realistic surface heat and salt fluxes should be included and the use of extrapolated climatological winds needs to be upgraded to incorporate synoptic winds to improve realism.

References

Blumberg, A. F. and G. L. Mellor (1987): A description of a three-dimensional coastal ocean circulation model. p. 1–16. In *Three Dimensional Coastal Ocean Models*, ed. by N. S. Heaps, American Geophysical Union.

Cheang, B. K. (1987): Short- and long-range monsoon prediction in southeast Asia. p. 579–606. In *Monsoons*, ed. by J. S. Fein and P. L. Stephens, John Wiley & Sons Inc., New York.

Chu, P. C. and C. P. Chang (1997): South China Sea warm pool in boreal spring. *Adv. Atmos. Sci.*, **14**, 195–206.

Chu, P. C., H. C. Tseng and C. P. Chang (1996): South China Sea warm-core and cold-core eddies detected from the Navy's Master Oceanographic Observational Data Set. p. 176–180. In *Proceedings on the Eighth Conference on Air-Sea Interaction*, American Meteorological Society.

Chu, P. C., H. C. Tseng, J. M., Chen and C. P. Chang (1997a): South China Sea warm pool detected from the Navy's Master Oceanographic Observational Data Set. *J. Geophys. Res.*, **102**, 15,761–15,771.

Chu, P. C., S. H. Lu and Y. C. Chen (1997b): Temporal and spatial variability of the South China Sea surface temperature anomaly. *J. Geophys. Res.*, **102**, 20,937–20,955.

Chu, P. C., C. Fan, C. J. Lozano and J. L. Kerling (1998): An airborne expandable bathythermograph survey of the South China Sea, May 1995. *J. Geophys. Res.* (in press).

Dale, W. L. (1956): Winds and drift currents in the South China Sea. *Malay. J. Trop. Geogr.*, **8**, 1–31.

Haney, R. L. (1971): Surface boundary conditions for ocean circulation models. *J. Phys. Oceanogr.*, **1**, 241–248.

Hellerman, S. and M. Rosenstein (1983): Normal monthly wind stress over the world ocean with error estimates. *J. Phys. Oceanogr.*, **13**, 1093–1104.

Levitus, S. and T. Boyer (1994): World Ocean Atlas, Vol 4: Temperature. *NOAA Atlas NESDIS*, **4**, U.S. Gov. Printing Office, Washington, D.C., 117 pp.

Levitus, S., R. Burgett and T. Boyer (1994): World Ocean Atlas, Vol 3: Salinity. *NOAA Atlas NESDIS*, **3**, U.S. Gov. Printing Office, Washington, D.C., 99 pp.

Mellor, G. and T. Yamada (1982): Development of a turbulence closure model for geophysical fluid problems. *Rev. Geophys. Space Phys.*, **20**, 851–875.

Metzger, E. J. and H. Hurlburt (1996): Coupled dynamics of the South China Sea, the Sulu Sea, and the Pacific Ocean. *J. Geophys. Res.*, **101**, 12,331–12,352.

Nitani, H. (1970): Oceanographic conditions in the sea east of Philippines and Lozon Strait in summer of 1965 and 1966. p. 213–232. In *The Kuroshio—A Symposium on Japan Current*, ed. by J. D. Mar, East-West Press, Honolulu.

Smagorinsky, J. (1963): General circulation experiments with the primitive equations. *Mon. Wea. Rev.*, **91**, 99–164.

South China Sea Institute of Oceanology, Academia Sinica (1985): p. 183–231. In *Integrated Investigation Report on Sea Area of the South China Sea (II)*, Science Press, Beijing.

Soong, Y. S., J. H. Hu, C. R. Ho and P. P. Niiler (1995): Cold-core eddy detected in South China Sea. *EOS Trans. AGU*, 345–347.

Uda, M. and T. Nakao (1972): Water masses and currents in the South China Sea and their seasonal changes. p. 161–188. In *The Kuroshio—Proceedings of the 3rd CSK Symposium*, Bangkok, Thailand.

Wyrtki, K. (1961): Scientific results of marine investigations of the South China Sea and the Gulf of Thailand 1959–1961. Naga Report, 2, University of California at San Diego, 195 pp.